Influence of a pulsed CO₂ laser operating at 9.4 µm on the surface morphology, reflectivity, and acid resistance of dental enamel below the threshold for melting

Jin Wan Kim
Raymond Lee
Kenneth H. Chan
Jamison M. Jew
Daniel Fried

Influence of a pulsed CO₂ laser operating at 9.4 μm on the surface morphology, reflectivity, and acid resistance of dental enamel below the threshold for melting

Jin Wan Kim, Raymond Lee, Kenneth H. Chan, Jamison M. Jew, and Daniel Fried*
University of California, San Francisco, San Francisco, California 94143-0758, United States

Abstract. Below the threshold for laser ablation, the mineral phase of enamel is converted into a purer phase hydroxyapatite with increased acid resistance. Studies suggest the possibility of achieving the conversion without visible surface alteration. In this study, changes in the surface morphology, reflectivity, and acid resistance were monitored with varying irradiation intensity. Bovine enamel specimens were irradiated using a CO₂ laser operating at 9.4 μm with a Gaussian spatial beam profile—1.6 to 3.1 mm in diameter. After laser treatment, samples were subjected to demineralization to simulate the acidic intraoral conditions of dental decay. The resulting demineralization and erosion were assessed using polarization-sensitive optical coherence tomography, three-dimensional digital microscopy, and polarized light microscopy. Distinct changes in the surface morphology and the degree of inhibition were found within the laser-treated area in accordance with the laser intensity profile. Subtle visual changes were noted below the melting point for enamel that appear to correspond to thresholds for denaturation of the organic phase and thermal decomposition of the mineral phase. There was significant protection from laser irradiation in areas in which the reflectivity was not increased significantly, suggesting that aesthetically sensitive areas of the tooth can be treated for caries prevention. © *2017 Society of Photo-Optical Instrumentation Engineers (SPIE)* [DOI: 10.1117/1.JBO.22.2.028001]

1 Introduction

Several developments are driving the shift to more conservative restorative dentistry and these include: new and more sensitive methods of caries detection, the development of new, more effective adhesive restorative materials, and the public's demand for more aesthetic restorations. Over the past 50 years, the nature of dental caries has changed, with the majority of new lesions occurring in the high-risk pits and fissures (occlusal surfaces) of posterior teeth. The enamel of the pits and fissures can be rendered more resistant to acid dissolution through thermal modification using CO₂ laser irradiation.[1–5] There are other high-risk sites that are located on tooth facial surfaces such as the areas around orthodontic appliances and near the gum line where there is increased plaque accumulation. These surfaces are more challenging to treat with the laser since any melting or roughening of the enamel that is visually apparent is undesirable. Therefore, it is important to understand how thermally induced morphological changes in enamel that occur below the melting threshold impact the reflectivity of enamel and its resistance to acid dissolution for the effective treatment of high-risk areas on tooth facial surfaces without adversely changing the appearance of the enamel.

At wavelengths between 9 and 11 μm where CO₂ lasers operate, enamel strongly absorbs laser energy resulting in the conversion of carbonated hydroxyapatite to a purer phase hydroxyapatite.[1–5] The strongest absorption by dental enamel

occurs near 9.6 μm, and CO₂ lasers operating between 9.3 and 9.6 μm are best suited for the thermal modification of enamel since lasers operating at these wavelengths require the minimum amount of laser energy for the thermal transformation.[6,7] At those wavelengths, the thermal relaxation time of the deposited energy is on the order of a few microseconds; therefore, microsecond pulse durations are desirable.[8] CO₂ lasers can be operated at high-repetition rates and have been integrated with laser scanning systems for highly uniform treatment of tooth surfaces.[9,10]

Optical coherence tomography (OCT) is capable of monitoring the severity of tooth demineralization and erosion.[11–14] Previous studies have also shown that there are distinct advantages of using polarization-sensitive OCT (PS-OCT) to measure the severity of subsurface demineralization in enamel and dentin and that it is well suited for this role.[12,15–21] Since OCT measures the changes in the reflectivity of the enamel, it is capable of measuring both changes in the enamel due to thermal modification by laser irradiation and changes in the reflectivity due to acid demineralization.

In a previous study, we demonstrated that PS-OCT could be used to nondestructively assess caries inhibition after carbon dioxide laser irradiation and the application of topical fluoride.[22] PS-OCT was used to measure the integrated reflectivity of the lesion area, and it was significantly lower in the laser- and fluoride-treated areas. We also found that the laser irradiation alone

---

caused changes in the reflectivity of the enamel and caused an increase in the integrated reflectivity from those areas. This interfered with the assessment of the severity of the enamel lesions but was not large enough to resolve significant differences between the treated and untreated groups. It appeared that at irradiation intensities below the melting threshold for enamel at the "wings" of the laser-treated zones where there were minimal changes in enamel reflectance, the laser was still effective in inhibiting demineralization. The purpose of this study was to follow up on that prior study using a new RF-excited laser operating at 9.4 μm that is capable of generating short 26-μs laser pulses with high single-pulse energies (>100 mJ) delivered at high-pulse repetition rates. With the Gaussian spatial profile and the high single-pulse energies, a large laser beam diameter can be used, allowing investigation of the changes induced over a continuously varying laser intensity profile. In this study, we closely examined the relationship between changes in the enamel surface morphology and the degree of resistance to acid dissolution with variation in the laser intensity profile. We employed a high-resolution (1000× magnification) digital microscope that is capable of acquiring images of the surface morphology of laser-irradiated tooth surfaces through depth convolution imaging. This approach is advantageous over scanning electron microscopy, which requires a high-vacuum environment that can induce morphological changes in dental enamel such as the formation of microcracks. PS-OCT was used to detect changes in the reflectivity of laser-treated surfaces and to assess the degree of inhibition to acid dissolution. In this study, we discovered that there are subtle changes in the enamel surface morphology below the melting threshold of enamel, including a slight increase in reflectivity and the formation of microcracks (crazing). Multiple dissolution studies indicated that significant acid resistance was imparted to the enamel without creating large changes in the optical appearance and enamel reflectivity.

2 Materials and Methods

2.1 Laser Irradiation Parameters

An RF-excited laser prototype Diamond J5-V from Coherent (Santa Clara, California) operating at a wavelength of 9.4 μm was used with a pulse duration of 26 μs and pulse repetition rates of up to 3 kHz. The laser had a Gaussian-shaped spatial profile. The laser energy output was monitored using a power/energy meter, ED-200 from Gentec (Quebec, Canada). The laser beam was focused to a beam diameter of 1.6 or 3.1 mm using a ZnSe scanning lens of $f = 125$ mm. A razor blade was scanned across the beam to determine the diameter ($1/e^2$) of the laser beam. A computer-controlled high-speed motion control system with Newport (Irvine, California) UTM150 and 850G stages and an ESP300 controller was used to create controlled movement of the samples during laser irradiation. Samples were scanned across the laser beam at the rate of 1 to 2 mm/s, and the pulse repetition rate was varied. Incisions approximately 150 μm in diameter separating the windows were created using the same laser system with a $f = 25$-mm aspheric ZnSe lens. A low-volume/low-pressure air-actuated fluid spray delivery system consisting of a 780S spray valve, a Valvemate 7040 controller, and a fluid reservoir from EFD, Inc. (East Providence, Rhode Island) was used to provide a uniform spray of fine water mist onto the tooth surfaces at 2 mL/ min.
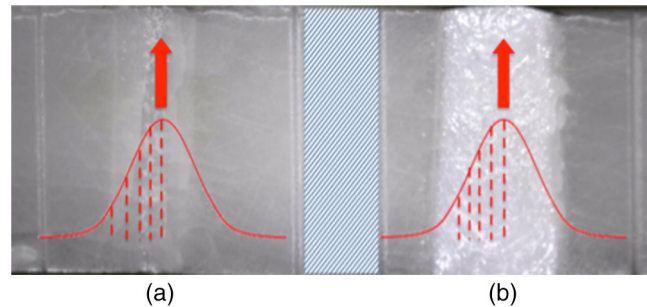

Fig. 1 Bovine enamel block with two treatment windows and a superimposed diagram of the incident fluence distribution for different irradiation parameters. The fluence on (a) was 1.6 J/cm^2 while the fluence on (b) was 2.6 J/cm^2. A 100-Hz repetition rate and a scanning speed of 2 mm/s were used.

2.2 Sample Preparation

Three sets of bovine blocks were used in the study. Blocks approximately 10 mm in length, 2 mm in width, with a remaining enamel thickness of at least 500 μm on the surface were prepared from extracted tooth incisors acquired from a slaughterhouse. For the first set of 16 blocks, each enamel sample was partitioned into three regions or windows (two laser irradiated and one protected) by etching 150-μm wide incisions between windows (see Fig. 1). The left window was irradiated with 1.6 J/cm^2, and the right window was irradiated with a fluence of 2.6 J/cm^2. A scanning rate of 2 mm/s was used for the first group of samples. A thin layer of acid-resistant varnish, red nail polish, Revlon (New York, New York) was applied to protect the sound enamel control area during exposure to the dissolution solution. The first set of samples was immersed in a surface softened demineralization solution composed of a 40-mL aliquot of 2.0-mmol/L calcium, 2.0-mmol/L phosphate, and 0.075-mol/L acetate at pH 4.8 at 37°C for 48 h. After exposure, the acid-resistant varnish was removed with acetone and then scanned with PS-OCT. The resulting demineralization for the first set of samples after 48 h was somewhat severe, causing erosion of the unprotected areas outside the laser-treated zone.

Two more sets of bovine blocks were irradiated and exposed to a less severe acid challenge to avoid erosion. The same demineralization solution described above was used with a pH 5.0. In addition, topical fluoride was also added to the left side of the block and the same laser irradiation parameters were applied to both the left and right windows. Topical fluoride has been found to interact synergistically with laser irradiation to inhibit acid dissolution, but the mechanism of synergistic interaction is not known.[22-26] For the later two sets of blocks, the protected windows were located on the extreme left and right sides of the blocks and there was no protected window in the center. In the second set of 20 bovine blocks, a fluence of 0.9 J/cm^2 was used with a laser scanning rate of 1 mm/s and a spot diameter of 3.1 mm, so a narrow melt zone was created at the center of the laser profile similar to what is shown in Fig. 1(a) for the blocks in set 1. In the third set, a fluence of 0.9 J/cm^2 was used with a laser scanning rate of 2 mm/s, which did not produce a continuous melt zone at the center of the laser spot. The area was irradiated by two laser scans separated by 250 μm to create a larger area similar to area 3 shown in Fig. 2, which is below the melting threshold; however, microcracks were clearly visible in the surface. Acidulated phosphate
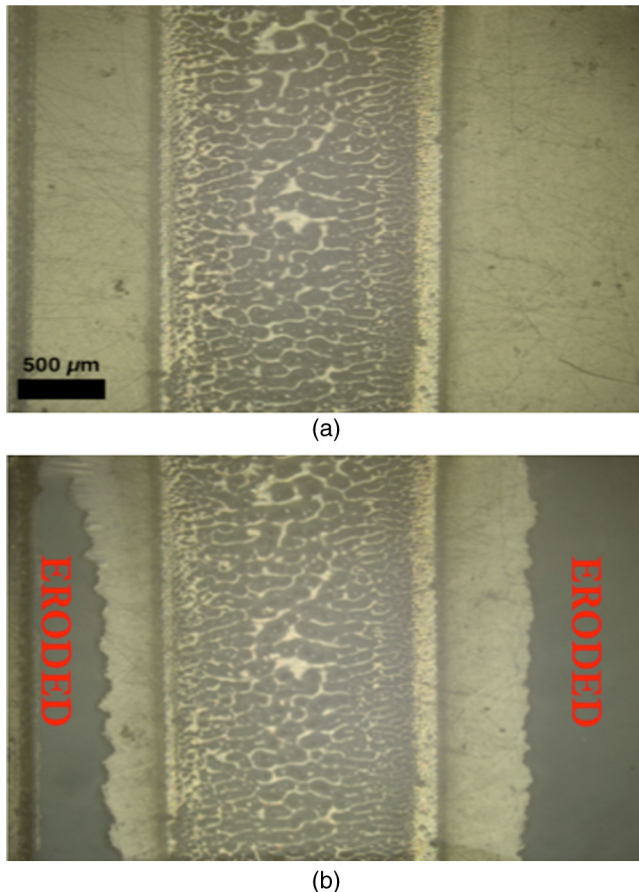
Fig. 2 Depth convolution images (a) after laser irradiation and (b) after exposure to the demineralization solution. Sample was irradiated with a fluence of 2.6 J/cm², 100-Hz repetition rate, and a scanning speed of 2 mm/s.

fluoride gel 1.23% from Keystone (Gibbstown, New Jersey) was added to the left side of each of the samples in the second and third sets for 1 min, and it was rinsed off with water. The same surface dissolution model was applied at 24-h intervals at a higher pH 5.0 to avoid erosion, and OCT scans were taken after every 24 h, so images could be acquired before erosion if erosion did occur. After 72 h, subsurface lesions approximately 100-μm deep were produced with an intact surface and without erosion, as can be seen in the polarized light microscopy (PLM) images of Fig. 5.

2.3 Digital Microscopy

Images of the tooth occlusal surfaces were examined using a digital microscopy/three-dimensional surface profilometry system, the VHX-1000 from Keyence (Elmwood, New Jersey) with the VH-Z25 and VH-Z100R lenses with a magnification from 25× to 1000×. Images were acquired by scanning the image plane of the microscope and reconstructing a depth composition image with all points at optimum focus displayed in a two-dimensional (2-D) image.

2.4 Polarization-Sensitive Optical Coherence Tomography System

An all-fiber-based optical coherence-domain reflectometry system with polarization-maintaining optical fiber, high-speed

piezoelectric fiber stretchers, and two balanced InGaAs receivers that was designed and fabricated by Optiphase, Inc., Van Nuys, California was used. This two-channel system was integrated with a broadband superluminescent diode (SLD) Denselight (Jessup, Maryland) and a high-speed XY-scanning system, ESP-300 controller, and 850G-HS stages from Newport for *in vitro* OCT. This system is based on a polarization-sensitive Michelson white light interferometer. The high-power (15 mW) polarized SLD source operated at a center wavelength of 1317 nm with a spectral bandwidth full-width at half-maximum of 84 nm. The sample arm was coupled to an anti-reflection (AR)-coated fiber collimator to produce a 6 mm in diameter collimated beam. That beam was focused onto the sample surface using a 20-mm focal length AR-coated planoconvex lens. This configuration provided a lateral resolution of approximately 20 μm and an axial resolution of 10 μm in air with a signal-to-noise ratio of greater than 40 to 50 dB. The PS-OCT system is completely controlled using Labview software from National Instruments (Austin, Texas). The system is described in greater detail in Refs. [27] and [28]. Acquired scans are compiled into b-scan files. Image processing was carried out using Igor Pro, data analysis software from Wavemetrics Inc. (Lake Oswego, Oregon).

2.5 Analysis of Polarization-Sensitive Optical Coherence Tomography Scans

We have developed automated methods[29–31] for determining the depth of demineralization (LD) and subsequently integrating the reflectivity in the cross-polarization image over that depth to calculate the integrated reflectivity with lesion depth, which we call ΔR. ΔR is analogous to the integrated mineral loss over lesion depth, ΔZ, measured with microradiography and is the gold standard for quantification of the severity of demineralization. The demineralization or lesion severity can be represented by 2-D projection maps of LD and ΔR. In this study, LD and ΔR maps were created for all the windows, both after laser irradiation and after exposure to the demineralization solution. Lineouts were extracted from the LD and ΔR maps at positions 0, 300, 600, 900, and 1200 μm from the center of the irradiated spot for comparing changes with laser intensity along the laser profile. If erosion was present, erosion depths were calculated by comparing the heights of the demineralized, laser treatment window and acid-resistant control. To account for the mineral lost to erosion for the set 1 samples, an estimated ΔR value for the erosion was added to the overall value for ΔR by multiplying the depth of erosion by the highest reflectivity in that particular a-scan. This adjustment was not necessary for the second and third sample sets since there was no erosion with those samples.

2.6 Polarized Light Microscopy

After sample imaging was completed, 200-μm-thick serial sections were cut using an Isomet 5000 saw (Buehler, Illinois), for PLM and transverse microradiography. PLM was carried out using a Model RZT microscope from Meiji Techno Co., LTD (Saitama, Japan) with an integrated digital camera, EOS Digital Rebel XT from Canon Inc. (Tokyo, Japan). The sample sections were imbibed in water and examined in the brightfield mode with crossed polarizers and a red I plate with 500-nm retardation. PLM images were acquired at 15× magnification.

3 Results

Digital microscopy images of one of the sample windows from the first set of bovine blocks are shown in Fig. 2 before and after exposure to the demineralization solution. The sample window irradiated at 2.6 J/cm^2 with a 100-Hz repetition rate and a scanning speed of 2 mm/s is shown. The melted zone is more extensive for the higher fluence and extends over most of the laser profile. After exposure to the demineralization solution, the unprotected areas were eroded while the laser-treated areas remained intact. The area melted by the laser remains relatively intact, and no changes are visually apparent. At about 200 to 500 μm beyond the melted area, there is erosion and loss of enamel due to acid dissolution. In between the eroded area and the melted area, there is a protected zone that remained intact.
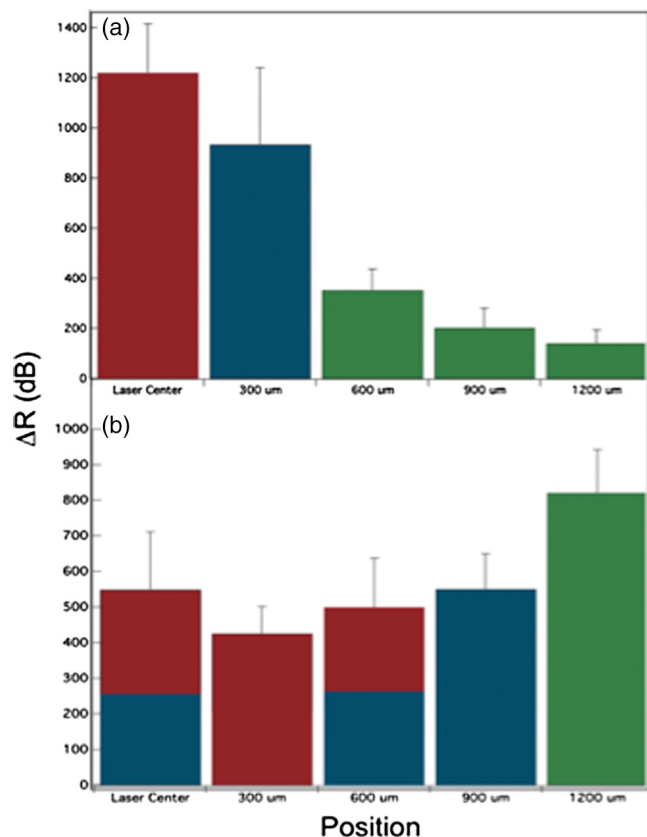
A high-resolution depth convolution digital microscopy image of the surface of one of the bovine blocks irradiated at 2.6 J/cm^2 with a 100-Hz repetition rate and a scanning speed of 2 mm/s is shown in Fig. 3, and there are four different zones of surface modification that are clearly visible. This image was taken after laser irradiation and before exposure to the demineralization solution. On the right side of the image (zone 4) at the center of the laser beam, the enamel has been completely melted, producing wave-like structures and a glazed appearance to the enamel. The wave-like structures have a modulation of $\pm$10 to 20 μm. In zone 3, the enamel appears whiter, the overall reflectivity is higher, and the enamel appears to be separated into large grains. The appearance is very similar to the dried mud in a dry lake bed. In zone 2, the craze lines are smaller, close inspection shows that the visibility of the enamel prism boundaries is enhanced as if they were etched, and the area appears darker due to the diffuse scattering at the prism boundaries. Zone 1 is unmodified enamel with no changes discernible.
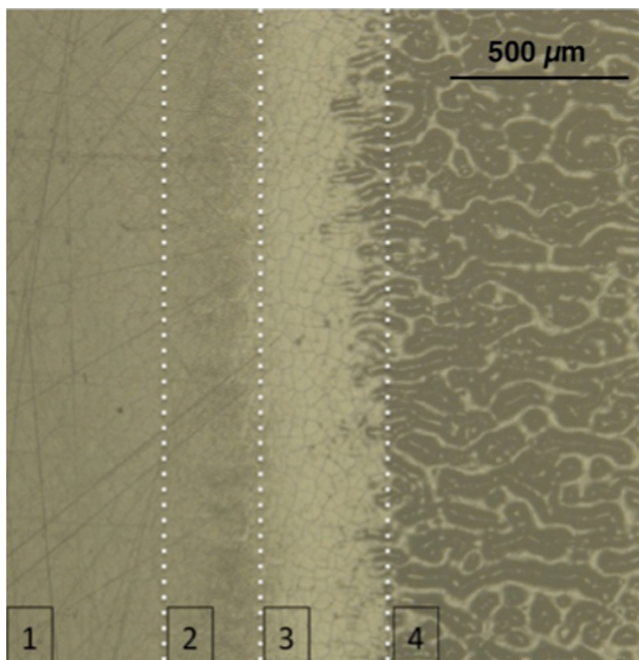
PS-OCT images of all the bovine blocks after laser irradiation and before exposure to the dissolution solution were acquired. The mean integrated reflectivity over the lesion depth $(\Delta R) \pm$ standard deviation is plotted for each position in Fig. 4 after laser irradiation and after exposure to the demineralization solution for the set 1 samples irradiated at 2.6 J/cm^2 with a 100-Hz repetition rate and a scanning speed of 2 mm/s. The values at each position were compared using repeated measures analysis of variance (RM-ANOVA). In the top plot representing the reflectivity changes created by the laser, the reflectivity is significantly higher than the nonirradiated area for the laser center and 300 μm from the center. After exposure to the demineralization, the laser-irradiated zones out to 900 μm had a significantly lower reflectivity than the nonirradiated zone (1200 μm), indicating that the areas with minimal surface modification (600 and 900 μm) provided significant protection against acid dissolution. It is important to note that the increase in ΔR caused by laser irradiation before exposure to acid dissolution cannot be subtracted from the overall increase in ΔR after dissolution to yield the increase in ΔR caused only by acid dissolution. Local asperities after laser irradiation likely are preferentially dissolved, reducing the surface roughness. In fact, the mean ΔR at the laser center is lower after acid dissolution than it is before.

A 2-D surface projection image of ΔR, the integrated reflectivity in the cross-polarization OCT image over the lesion depth, is shown in Fig. 5 for one of the samples from the second group of bovine blocks (set 2) after exposure to the dissolution


Fig. 3 Depth convolution image showing different surface modifications from the center of the laser profile (4) to unaffected area (1). Sample was irradiated with a fluence of 1.6 J/cm^2 with a 100-Hz repetition rate and a scanning speed of 2 mm/s.

Fig. 4 Measured mean integrated reflectivity $\pm$ S.D. (a) before and (b) after laser irradiation and exposure to the demineralization solution with varying distance from the laser center. Bars of the same color are statistically similar ($P > 0.05$). There were eight samples per group.
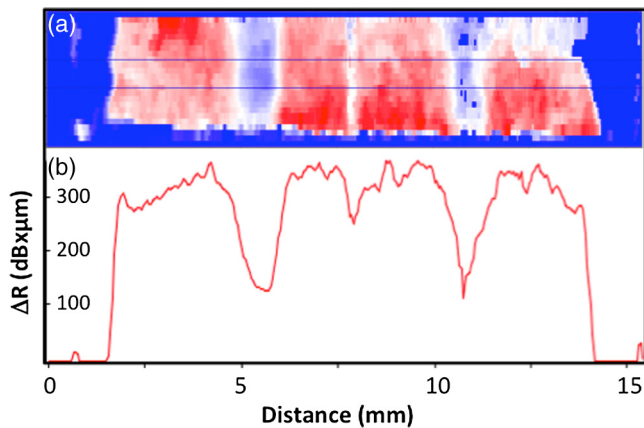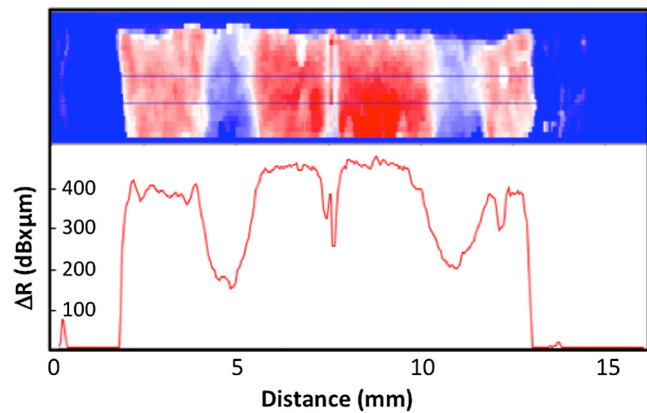
Fig. 5 (a) 2-D projection image of the integrated reflectivity with lesion depth (ΔR) from a bovine block after exposure to the demineralization solution for an incident fluence of 0.9 J/cm^2, a spot diameter of 3.1 mm, a 100-Hz repetition rate, and a scanning speed of 1 mm/s. A red-white-blue intensity scale is used, where red is higher reflectivity. (b) The mean ΔR values in the window between the two lines are plotted.

Fig. 6 (a) 2-D projection image of ΔR from a bovine block after exposure to the demineralization solution for an incident fluence of 0.9 J/cm^2, a spot diameter of 3.1 mm, a 200-Hz repetition rate, and a scanning speed of 2 mm/s. Two overlapping spots separated by 250 μm were used. A red-white-blue intensity scale is used, where red is higher reflectivity. (b) The mean ΔR values in the window between the two lines are plotted.

solution. That set was irradiated at a fluence of 0.9 J/cm^2 with a laser scanning rate of 1 mm/s and a spot diameter of 3.1 mm, so a narrow melt zone was created at the center of the laser profile. Higher values for ΔR represent more severe demineralization and are shown in red, while the areas protected by laser irradiation are shown in blue. Mean ΔR values for the area between the lines are plotted below the 2-D projection image. The reduction in the lesion severity follows the Gaussian profile of the laser intensity profile. There does not appear to be any effect of the topical fluoride on inhibiting acid dissolution, and the lesion severity appears similar on both sides of the sample. The small central peak is due to the protection peripheral to the laser incision separating the two windows. The mean values for ΔR at the center of each window for the second set ($n = 20$) were 439 ± 47 for the control window, 445 ± 104 for fluoride only, 323 ± 49 for laser only, and 362 ± 69 for laser and fluoride. The sample groups were compared using RM-ANOVA, and the means for the control and fluoride groups were significantly higher ($P < 0.05$) than for the two laser groups, but neither the laser groups (L, L + F) nor nonlaser groups (C, F) were significantly different from each other.

A 2-D surface projection image of ΔR is shown in Fig. 6 for one of the samples from the third group of bovine blocks (set 3) after exposure to the dissolution solution. That set was irradiated at a fluence of 0.9 J/cm^2 with a laser scanning rate of 2 mm/s and a spot diameter of 3.1 mm, and there were two parallel scans offset by 250 μm to create a flatter intensity profile without a definitive melt zone. For this sample, the profile of the protected area is larger and not as sharply peaked as in Fig. 5, reflecting the flatter intensity profile. The mean values for ΔR at the center of each window for the third set ($n = 20$) were 417 ± 105 for the control window, 458 ± 72 for fluoride only, 236 ± 126 for laser only, and 253 ± 138 for laser and fluoride. The sample groups were compared using RM-ANOVA, and the means for the control and fluoride groups were significantly higher ($P < 0.05$) than for the two laser groups, but neither the laser groups nor nonlaser groups were significantly different from each other.

PLM images of two thin sections cut from samples from the second and third sets of bovine blocks are shown in Fig. 7.
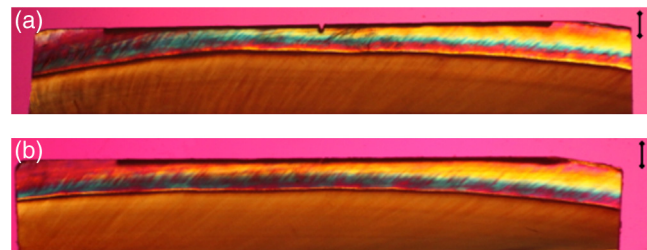
Fig. 7 Polarized microscopy image of 200-μm-thick sections for groups 1 and 2 after exposure to the demineralization solution for an incident fluence of 0.9 J/cm^2 and a spot diameter of 3.1 mm: (a) 100-Hz repetition rate and a scanning speed of 1 mm/s and (b) 200-Hz repetition rate and a scanning speed of 2 mm/s with two overlapping spots separated by 250 μm. The bars on the upper right corner of each image are 500 μm.

Strong light scattering from the lesion area depolarizes the light, and the lesion areas appear black. The lesions range from 50- to 100-μm deep, and there are no lesions on the extreme ends of each section where the area was protected with acid-resistant varnish. The laser incision separating the left and right groups can be seen in the center of each section. The influence of the laser-treated zones and fluoride is not as obvious in the PLM images as it is in the 2-D projection images of ΔR (Figs. 4 and 5). Although the depth of demineralization can be clearly resolved in PLM images, it is difficult to resolve differences in the severity of demineralization in PLM images.

4 Discussion

This is the first study employing high-resolution digital microscopy to image the subtle surface morphological changes produced during the laser irradiation of dental enamel. Depth convolution images are valuable for examining rough surfaces such as laser-irradiated dental enamel. Scanning electron microscopy has been used extensively to study laser-irradiated tooth surfaces and shows the melted structures on enamel surfaces quite well.[32–34] However, samples were placed in a vacuum and subtle effects such as the crazing, microcracks, and dehydration observed in the second and third zones in Fig. 3 may not

be evident and, if observed, may be attributed to placing the samples in the high-vacuum environment. A fairly large laser beam diameter was used in this study and the laser was scanned laterally, so the effects of variations in the enamel surface temperature could be observed over greater distances, which may also explain why the subtle surface changes were not observed in previous studies.

Thermal analysis studies have shown that enamel melts at 1200°C and that thermal decomposition of carbonated hydroxyapatite to purer phase hydroxyapatite occurs at 420°C.[35] These changes are expected to increase the acid resistance of enamel.[1,36] In addition, changes to protein and lipid, such as denaturation, take place at much lower temperatures, above 80°C.[37,38] It is likely that the central melt zone, zone 4 in Fig. 3, represents temperature excursions exceeding 1200°C, which is necessary to produce melting. Zone 3 likely represents temperatures exceeding 420°C, which is sufficient for inducing the thermal decomposition of carbonated hydroxyapatite to a purer phase hydroxyapatite with the evolution of carbon dioxide and water. The transformation of carbonated hydroxyapatite to a purer phase hydroxyapatite results in a more compact crystal lattice, and that lattice contraction is likely responsible for the microcracks and granular changes visible in zone 3 in Fig. 3. The purer hydroxyapatite has a higher crystallinity and is more resistant to acid dissolution. It is important to point out that these enamel microcracks are extremely small and localized to the outer few microns of enamel and are not large enough to influence the structural integrity of the tooth. Since such changes are observable optically and they demarcate the threshold needed to inhibit acid dissolution, observation of the formation of the microcracks may provide a means for visual confirmation of successful treatment of the enamel *in vivo*. In addition, alternative explanations for thermal decomposition have been provided to explain the mechanism of caries inhibition by carbon dioxide laser radiation,[39] and our observations clearly provide evidence that favors decomposition of carbonated hydroxyapatite to a purer phase hydroxyapatite. Protein and lipids are concentrated at the prism boundaries, so it is likely that enhancement of the prism boundaries in area 2 occurs at temperatures between 80 and 420°C and it does appear that the magnitude of the changes varies considerably across area 2, with the right side of the zone considerably darker than the left side.

The principal advantage of using PS-OCT is that it is nondestructive and can be used *in vivo* to assess lesion severity. However, modification of the surface morphology of the enamel due to laser irradiation also increases the reflectivity in a similar fashion to demineralization. Therefore, that modification can interfere with the ability of PS-OCT to assess changes in the lesion severity. We have already demonstrated in a previous study that the interference is not so great that it prevents the use of OCT for assessing the inhibition of acid dissolution on laser-irradiated surfaces.[22] However, in this study, we also assessed the increase in ΔR caused by modification of the laser and used those values to identify the position of the laser-treated zones (Fig. 3). Identifying laser intensity thresholds that inhibit acid dissolution but do not cause large changes in reflectivity is important for the treatment of tooth buccal surfaces where any changes in reflectivity is undesirable for aesthetic reasons. The areas surrounding orthodontic brackets are at high risk for dental decay due to plaque accumulation; treating those areas with the laser would be desirable for inhibiting that decay, but any visible

changes would be unacceptable. In this study, we clearly show that inhibition is possible without melting the enamel surface and that the changes induced in the enamel surface morphology only cause small changes in the enamel reflectivity.

The lack of efficacy of topical fluoride in this study was unanticipated, and we have no explanation for the lack of effect. We had anticipated that the fluoride would stick to the prism boundaries and microcracks formed in zones 2 and 3 and that a positive result would provide an explanation for the synergistic effect that has previously been observed for laser irradiation and fluoride. The effect of topical fluoride was observed in our previous enamel dissolution studies, and we were previously able to differentiate the effect using PLM. This was the first time we employed a topical fluoride gel as opposed to a topical fluoride foam, but both systems should behave similarly.[22]

In summary, there was significant protection from the laser in areas that were not visually altered. By utilizing the laser beam intensity profile, we were able to identify the incident fluence necessary for protection while not markedly altering the surface reflectivity. Subtle surface changes were noted, demarcating enamel temperature changes and transformation of the organic and mineral constituents of enamel below the threshold for melting.

Disclosures

No conflicts of interest, financial or otherwise, are declared by the authors.

Acknowledgments

References

1. B. Fowler and S. Kuroda, "Changes in heated and in laser-irradiated human tooth enamel and their probable effects on solubility," *Calcif. Tissue Int.* **38**, 197–208 (1986).
2. J. D. B. Featherstone and D. G. A. Nelson, "Laser effects on dental hard tissue," *Adv. Dent. Res.* **1**(1), 21–26 (1987).
3. D. G. A. Nelson, W. L. Jongebloed, and J. D. B. Featherstone, "Laser irradiation of human dental enamel and dentine," *N. Z. Dent. J.* **82**, 74–77 (1986).
4. J. D. B. Featherstone et al., "CO_2 laser inhibition of artificial caries-like lesion progression in dental enamel," *J. Dent. Res.* **77**(6), 1397–1403 (1998).
5. D. Fried et al., "Dental hard tissue modification and removal using sealed TEA lasers operating at $\lambda = 9.6$ μm," *J. Biomed. Opt.* **6**(2), 231–238 (2001).
6. M. Zuerlein et al., "Optical properties of dental enamel at 9-11 μm derived from time-resolved radiometry," *IEEE J. Sel. Top. Quantum Electron.* **5**(4), 1083–1089 (1999).
7. M. Zuerlein, D. Fried, and J. D. B. Featherstone, "Modeling the modification depth of carbon dioxide laser treated enamel," *Lasers Surg. Med.* **25**, 335–347 (1999).
8. M. J. C. van Gemert and A. J. Welch, "Time constants in thermal laser medicine," *Lasers Surg. Med.* **9**, 405–421 (1989).
9. D. Fried et al., "Dissolution studies of bovine dental enamel surfaces modified by high-speed scanning ablation with a $\lambda = 9.3$ μm TEA CO_2 laser," *Lasers Surg. Med.* **38**(9), 837–845 (2006).
10. S. Assa, S. Meyer, and D. Fried, "Ablation of dental hard tissues with a microsecond pulsed carbon dioxide laser operating at 9.3-μm with an integrated scanner," *Proc. SPIE* **6843**, 684308 (2008).

11. B. T. Amaechi et al., "Use of optical coherence tomography for assessment of dental caries," *J. Oral Rehabil.* **28**(12), 1092–1093 (2001).
12. D. Fried et al., "Early detection of dental caries and lesion progression with polarization sensitive optical coherence tomography," *J. Biomed. Opt.* **7**(4), 618–627 (2002).
13. D. Fried et al., "Early caries imaging and monitoring with near-IR light," *Dent. Clin. North Am.* **49**(4), 771–793 (2005).
14. T. Louie et al., "Clinical assessment of early tooth demineralization using polarization sensitive optical coherence tomography," *Lasers Surg. Med.* **42**, 898–905 (2010).
15. A. Baumgartner et al., "Polarization-sensitive optical coherence tomography of dental structures," *Caries Res.* **34**, 59–69 (2000).
16. P. Ngaotheppitak, C. L. Darling, and D. Fried, "Polarization optical coherence tomography for the measuring the severity of caries lesions," *Lasers Surg. Med.* **37**(1), 78–88 (2005).
17. R. S. Jones et al., "Imaging artificial caries on the occlusal surfaces with polarization-sensitive optical coherence tomography," *Caries Res.* **40**(2), 81–89 (2006).
18. R. S. Jones and D. Fried, "Remineralization of enamel caries can decrease optical reflectivity," *J. Dent. Res.* **85**(9), 804–808 (2006).
19. H. Kang et al., "Nondestructive assessment of early tooth demineralization using cross-polarization optical coherence tomography," *IEEE J. Sel. Top. Quantum Electron.* **16**(4), 870–876 (2010).
20. A. M. Can et al., "Non-destructive assessment of inhibition of demineralization in dental enamel irradiated by a 9.3-μm CO_2 laser at ablative irradiation intensities with PS-OCT," *Lasers Surg. Med.* **40**(5), 342–349 (2008).
21. K. H. Chan et al., "A method for monitoring enamel erosion using laser irradiated surfaces and optical coherence tomography," *Lasers Surg. Med.* **46**(9), 672–678 (2014).
22. D. J. Hsu et al., "Nondestructive assessment of the inhibition of enamel demineralization by CO_2 laser treatment using polarization sensitive optical coherence tomography," *J. Biomed. Opt.* **13**(5), 054027 (2008).
23. C. Steiner-Oliveira et al., "Effect of a pulsed CO_2 laser and fluoride on the prevention of enamel and dentine erosion," *Arch. Oral Biol.* **55**(2), 127–133 (2010).
24. S. Tagomori and T. Morioka, "Combined effects of laser and fluoride on acid resistance of human dental enamel," *Caries Res.* **23**, 225–231 (1989).
25. J. Vlacic et al., "Laser-activated fluoride treatment of enamel against an artificial caries challenge: comparison of five wavelengths," *Aust. Dent. J.* **52**(2), 101–105 (2007).
26. C. R. Wheeler et al., "Irradiation of dental enamel with Q-switched 355-nm laser pulses: surface morphology, fluoride adsorption, and adhesion to composite resin," *Lasers Surg. Med.* **32**(4), 310–317 (2003).
27. J. Bush, P. Davis, and M. A. Marcus, "All-fiber optic coherence domain interferometric techniques," *Proc. SPIE* **4204**, 71 (2000).
28. P. Ngaotheppitak et al., "PS-OCT of occlusal and interproximal caries lesions viewed from occlusal surfaces," *Proc. SPIE* **6137**, 61370L (2006).
29. K. H. Chan et al., "Use of 2D images of depth and integrated reflectivity to represent the severity of demineralization in cross-polarization optical coherence tomography," *J. Biophotonics* **8**(1–2), 36–45 (2015).
30. J. Arends, J. L. Ruben, and D. Inaba, "Major topics in quantitative microradiography of enamel and dentin: R parameter, mineral distribution visualization, and hyper-remineralization," *Adv. Dent. Res.* **11**(4), 403–414 (1997).
31. M. H. Le, C. L. Darling, and D. Fried, "Automated analysis of lesion depth and integrated reflectivity in PS-OCT scans of tooth demineralization," *Lasers Surg. Med.* **42**(1), 62–68 (2010).
32. J. Palamara et al., "The effect on the ultrastructure of dental enamel of excimer-dye, argon-ion and CO_2 lasers," *Scanning Microsc.* **6**(4), 1061–1071 (1992).
33. J. Palamara et al., "The ultrastructure of human dental enamel heat-treated in the temperature range 200°C to 600°C," *J. Dent. Res.* **66**(12), 1742–1747 (1987).
34. S. M. McCormack et al., "Scanning electron microscope observations of CO_2 laser effects on dental enamel," *J. Dent. Res.* **74**(10), 1702–1708 (1995).
35. D. W. Holcomb and R. A. Young, "Thermal decomposition of human tooth enamel," *Calcif. Tissue Int.* **31**, 189–201 (1980).
36. S. Kuroda and B. O. Fowler, "Compositional, structural and phase changes in in vitro laser-irradiated human tooth enamel," *Calcif. Tissue Int.* **36**, 361–369 (1984).
37. J. Pearce and S. Thomsen, "Rate process analysis of thermal damage," in *Optical-Thermal Response of Laser-Irradiated Tissue*, A. J. Welch and M. J. C. van Gemert, Eds., pp. 487–550, Plenum, New York (1995).
38. A. J. Welch, "The thermal response of laser irradiated tissue," *IEEE J. Quantum Electron.* **20**(12), 1471–1481 (1984).
39. C. S. Hsu et al., "Effects of CO_2 laser and organic matrix on enamel demineralization," *J. Dent. Res.* **79**(9), 1725–1730 (2000).

Biographies for the authors are not available.